Numerical study of granular discharge flows through centred and off-centred rectangular hoppers using discrete element simulations

Jianhua Fan, Hongwei Wang, Li-Hua Luu, Pierre Philippe, Lu Wang, Zhen-Lei Wei, Jianqun Yu

Numerical study of granular discharge flows through centred and off-centred rectangular hoppers using discrete element simulations

Jianhua Fan[a,b], Hongwei Wang[a], Li-Hua Luu[c], Pierre Philippe [c], Lu Wang[d*], Zhen-lei Wei[b*]，Jianqun Yu[e]

[a] *School of Mechanical and Aerospace Engineering, Jilin University, Changchun 130025, China*

[b]*State Key Laboratory of Geohazard Prevention and Geoenvironment Protection, Chengdu University of Technology, Chengdu, 610059, China*

[c] *RECOVER, INRAE Aix-Marseille University, 3275 Route de Cézanne, 13182 Aix-en-Provence, France*

[d]*College of Food Science and Engineering, Jilin University, Changchun, 130062, China*

[e] *School of Biological and Agricultural Engineering, Jilin University, Changchun 130022, China*

Corresponding Author: E-mail address: luwang@jlu.edu.cn (Lu Wang)

Tel:+8618166881736

weizhenlei@cdut.edu.cn (Zhen-lei Wei)

Abstract: Gravity-driven particle flow through outlets with inclined angles and outlets with off-centred positions is investigated numerically by discrete element simulations. The measured particle discharge rates are well fitted by Beverloo's law, demonstrating a fairly linear relationship with orifice size to a power 3/2. The impacts of the hopper angle and the eccentric position of the outlet on the particle velocity and orifice volume fraction distribution are systematically investigated. The particle velocity and volume fraction distributions for different hopper angles are found to exhibit self-similar features that are well described by a mixed parabolic and power law with fractional exponents. The coefficients involved in determining the particle velocity and volume fraction distribution have clear physical significance. In the case of hopper angles in the range of 55° - 90°, the values of these determining coefficients are quite similar at each angle, leading to identical discharge rates of particles. The predicted mass flow rate derived from the velocity and volume fraction curves is found to be in satisfactory agreement with that obtained in the experimental works of Mendez *et al.* (2021) and Darias *et al.* (2020). Regarding the hopper with an eccentrical outlet, an asymmetry behavior appears. Moreover, the outlet directly at a wall generates a significantly higher flow rate than other locations. In the end, an extension of the self-similarity laws is proposed to allow the prediction of granular discharge for the rectangular hopper, from the centred to the border outlet case.

Keywords: Rectangular hopper, Hopper angle, Eccentricity, Discharge rate

1. Introduction

Granular flow widely exists in many industrial fields and natural phenomena. A well-known example is that of the discharge of a large number of solid particles from a hopper, for example, silo discharge for dry particles and the sinkhole formation related to the natural hazard where interstitial fluid has been involved [1,2]. Particle discharge is one of the important physical processes to handle since it is critical to the macroscopic flow behavior. Factors affecting the discharge rate include hopper geometry and particle properties, such as the particle friction coefficient, particle shape and size [3–6]. Although the simplest way to control the particle flow rate is to vary the outlet size, several additional factors, such as hopper angle, outlet position, and presence of an obstacle are easily adjusted in practice [7–10]. Nevertheless, a unified mathematical expression relevant to particle flow rate, hopper angle, off-centred shift, and orifice size is still lacking. In addition, hopper flow characteristics at the microscale are poorly understood.

Gravity-driven dense granular flow can be generally divided into three regimes: continuous flow, intermittent flow, and complete blockage of the flow due to the formation of an arch [11,12]. For the continuous flow regime, Beverloo [13] developed a widely used formula for predicting the discharge rate W (kg/s) at which particles are evacuated from a flat-bottomed cylindrical hopper with a circular outlet:

$$W = C\rho_b\sqrt{g}(D - kd)^{\mathrm{Dim}-1/2} \tag{1}$$

where ρ_b is the bulk density of the particles, D is the orifice size of the hopper and d is the particle diameter, C and k are fitting parameters for 2D case ($\mathrm{Dim} = 2$) and 3D case ($\mathrm{Dim} = 3$), respectively. Available studies have shown that k is related to the shapes and sizes of the particles, its value was found to be k=1.5 for spherical particles [14] and k=2.9 for sand [13]. Parameter C depends on the coefficient of friction between particles, usually in the range of $0.55 < C < 0.65$ [15–17]. However, this empirical formula is not valid when $D/d < 6$ [18]. Myers and Sellers [19] extended the Beverloo law to a rectangular hopper outlet with length L and width Z (hopper

angle 90°), and the discharge rate of particles is written as:

$$W = 1.03\rho_b\sqrt{g}(L - kd)(Z - kd)^{3/2} \quad (2)$$

Although the flow from the flat bottom rectangular hopper is $(Z - kd)^{3/2}$ and the cylindrical hopper is $(D - kd)^{5/2}$, the two formulas have consistent dimensions due to the $(L - kd)$ factor. This is also rather consistent with the quasi-2D experimental results where the exponent falls from 5/2 to 3/2 [20].

Only a few studies found that the hopper angle had a significant impact on the particle flow rate [15–17]. A granular analysis related to the flow rate by integrating the hopper angle was performed by Brown and Richards [21,22] who assumed that there was an arch above the orifice from which the particles fall freely (called Free Fall Arch (FFA)). Under the minimum energy assumption, Brown gave a flow expression [22]:

$$W(\alpha) = \left[\frac{\int_0^\alpha \sqrt{\cos\chi}\, d\chi}{\sin^{3/2}\alpha}\right]\rho_b\phi_B\sqrt{2g}l(D - kd)^{3/2} \quad (3)$$

where α represents the hopper angle, $\int_0^\alpha \sqrt{\cos\chi}\, d\chi$ is a function of α, and l denotes the layer depth. ϕ_B is the bulk volume fraction.

Apart from the hopper angle, the location of the outlet may cause unexpected behavior such hopped flow. A recent study by Bhateja *et al*. [23] showed that particle flow in a hopper with eccentrically located outlets resulted in asymmetrical discharge processes and different flow patterns. Maiti *et al*. [24] observed slip flow on the vertical wall of a hopper with eccentric outlets, and they proposed a kinematic model with slip boundary conditions for particle discharge. The simulation results were in good agreement with their own experiments. Wang *et al*. [25] developed an expression based on the Beverloo equation for predicting the discharge rate from discrete element simulations of rectangular hoppers with different eccentricities. Although much research related to hopper flow has been carried out, relatively few studies have examined the influence of eccentricity on the dynamics of particle flow. Moreover, the few existing corrections cannot be directly employed to predict the discharge rate from a rectangular hopper with outlets in eccentrical locations.

For dense particle flow, the discrete element method (DEM) is an ideal approach for studying the complex behavior of granular material [2,6,26–31] . Anand *et al*. [15] used DEM to study the influence of particle characteristics and hopper geometry on the granular flow. The results imply that the discharge rate significantly depends on the outlet size and hopper angle. Additionally, Liu *et al*. [32] numerically simulated the flow of elliptical particles in a flat-bottomed cylindrical hopper by DEM. They found that the larger the aspect ratio of elliptical particles was, the slower the flow rate. Ji *et al*. [33] investigated particle flow driven by the external pressure and showed that the discharge rate increased with increasing external pressure. Moreover, Zhang *et al*. [34] used DEM to investigate the discharge features of bidisperse particles in a rectangular hopper with an inclined bottom, they reported that the impact of hopper width on the discharge rate was minimal and the particle size ratio was proportional to the funnel flow, which is in agreement with their experiments.

In this study, we apply DEM to carry out a series of simulations to numerically investigate the influences of hopper angles and outlet location on the velocity and volume fraction profiles in 2D. The numerical DEM method, including Hertz-Mindlin contact model, the setup and model validation are introduced in Sections 2 and 3, respectively. The dimensional analysis of the velocity and volume fraction profiles of the particle is discussed in Section 4. Then, new formulas for predicting the discharge rate of particle flow are obtained by combining two rescaled profiles for a flat-bottomed rectangular hopper. Finally, the conclusion and outlook are presented in Section 5.

2. Numerical method

The DEM considers the medium as a series of discrete and independent elements which have their own mass, velocity, contact properties, and whose motion is based on Newton's second law. The evolution of the entire medium is described by the displacement and mutual position of each discrete element. Particles interact via contacts which are described in the following by the Hertz-Mindlin contact model [29,33,34]. Each solid particle is driven by a total contact force $\boldsymbol{F}_i^c$, which is equal to the sum of the

contact forces over all interacting particles, and the gravitational force. Then the force $\boldsymbol{F_i}$ exerted on each solid particle is given by:

$$\boldsymbol{F_i} = m_i\boldsymbol{g} + \boldsymbol{F}_i^c = m_i\frac{d\boldsymbol{u_i}}{dt} \quad (\text{with } \frac{dx_i}{dt} = \boldsymbol{u}_i \ ) \tag{4}$$

where m_i, $\boldsymbol{x}_i$ and $\boldsymbol{u}_i$ are the mass, position and velocity of the particle, respectively. The explicit time integration with the Verlet algorithm is adopted to solve the particle position and velocity.

When two circular particles i and j located at positions $\boldsymbol{r_i}$ and $\boldsymbol{r_j}$ are in contact with each other, their contact produces an overlap:

$$\delta_{ij}^n = R_i + R_j - (r_i - r_j)\cdot\mathbf{n} > 0 \tag{5}$$

where R_i and R_j are the particle radii, $\mathbf{n}$ is a unit normal vector. Then the contact force $\boldsymbol{F}_i^c$ between two particles can be divided into a normal component $\boldsymbol{F}_{ij}^n$ and a tangential component $\boldsymbol{F}_{ij}^t$. The normal force $\boldsymbol{F}_{ij}^n$ consists of the Hertz elastic force $\boldsymbol{F}_{ij}^{ne}$ and the viscous force $\boldsymbol{F}_{ij}^{nv}$ [29,33,34]:

$$\begin{cases} \boldsymbol{F}_{ij}^{ne} = 4/3\,E^*(R^*)^{1/2}{\delta_{ij}^n}^{3/2} \\ \boldsymbol{F}_{ij}^{nv} = C_n\left(8m^*E^*\left(R^*\delta_{ij}^n\right)^{1/2}\right)^{1/2}\cdot\boldsymbol{v}_{ij}^n \end{cases} \tag{6}$$

where δ_{ij}^n is the normal overlap, C_n represents the normal damping coefficient, and $\boldsymbol{v}_{ij}^n$ denotes the normal relative velocity. The equivalent elastic modulus E^*, the equivalent particle radius R^* and the equivalent mass m^* are calculated as follows $\frac{1}{E^*} = \frac{1-{\nu_i}^2}{E_i} + \frac{1-{\nu_j}^2}{E_j}$, $\frac{1}{R^*} = \frac{1}{R_i} + \frac{1}{R_j}$, $\frac{1}{m^*} = \frac{1}{m_i} + \frac{1}{m_j}$, where υ_i and υ_j are the values of Poisson's ratio, E_i and E_j are the moduli of elasticity, m_i and m_j are the mass of particle i and j, respectively.

The tangential contact forces between neighboring particles are based on the Mindlin theory with reference to the Mohr-Coulomb law [35]. Thus, the tangential force $\boldsymbol{F}_{ij}^t$ is composed of the viscous force $\boldsymbol{F}_{ij}^{tv}$ and elastic force $\boldsymbol{F}_{ij}^{te}$, which are determined by [29,33]:

$$\begin{cases} \boldsymbol{F}_{ij}^{te} = \mu_s \left|\boldsymbol{F}_{ij}^{ne}\right| \left(1 - \left(1 - \min\left(\delta_t, \delta_{t,max}\right)/\delta_{t,max}\right)^{3/2}\right) \cdot \bar{\boldsymbol{t}} \\ \boldsymbol{F}_{ij}^{tv} = C_t \left(6\mu_s m^* \left|\boldsymbol{F}_{ij}^{ne}\right| \sqrt{1 - \min\left(\delta_t, \delta_{t,max}\right)}/\delta_{t,max}\right)^{1/2} \cdot \boldsymbol{v}_{ij}^t \end{cases} \tag{7}$$

where μ_s, C_t stands for the sliding friction coefficient, tangential damping coefficient, respectively. δ_t and $\boldsymbol{v}_{ij}^t$ are the displacement and relative velocity in tangential direction, and $\delta_{t,max} = \mu_s\,(2-\nu)/2(1-\nu) \cdot \delta_{ij}^n$, $\bar{\boldsymbol{t}}$ is the unit vector pointing to the tangential direction.

When there is relative rotation between particles, the moment $\boldsymbol{M_R}$ resulted from rolling friction can be obtained as follows:

$$\boldsymbol{M_R} = \mu_R R_i \left|\boldsymbol{F}_{ij}^n\right| \hat{\boldsymbol{\omega}}_{\boldsymbol{ij}} \tag{8}$$

where μ_R represents the rolling friction coefficient, and $\hat{\boldsymbol{\omega}}_{\boldsymbol{ij}}$ is the relative angular velocity between two contact particles, given by $\hat{\boldsymbol{\omega}}_{\boldsymbol{ij}} = \boldsymbol{\omega}_{\boldsymbol{ij}}/\left|\boldsymbol{\omega}_{\boldsymbol{ij}}\right|$.

The time step in Eq. (4) related to oscillation period during particles interaction should be appropriately selected to ensure the particle motion correctly. Consequently, in the Hertz–Mindlin contact model, the critical time step between particles is calculated as [36]:

$$t_{max} = \pi r_{min} \sqrt{\rho_p/G}/(0.163\nu + 0.8766) \tag{9}$$

where r_{min}, ρ_p are the minimum radii and density of the particles, G and υ represents shear modulus and Poisson's ratio, respectively. In the present DEM simulations, the time step is chosen smaller than $0.1\ t_{max}$ to avoid any instability of the numerical method.

3. Numerical configurations and model validation

Hoppers with two types of outlets are used for the present study. The first type is the outlet with an inclined angle. The hopper angle α is set to 15°, 30°, 55°, 75° or 90°, as depicted in Fig. 1 (a). The volume fraction of granular sample is around $\phi_B = 0.59$ for this case. The second type is the eccentric outlet, and its position is determined by e and s, respectively, as shown in Fig. 1 (b), where the volume fraction is $\phi_B =$

0.57. The granular sample consists of 3000 particles with diameter d = 3 mm. The hopper is defined by its length L = 100 mm and height H = 400 mm. The thickness of each hopper model is restricted to Z=1.01 d, a bit larger than the particle diameter. Therefore, the present numerical configuration is quasi-2D with spheres but no transverse motion due to small thickness. The hopper outlet size D is 18, 30, 45 or 60 mm. The DEM simulation parameters are selected based on previous simulation studies [2,37], which can obtain results consistent with related experiment (see next paragraph). All the values for solid particles and hopper geometry are listed in Table 1.

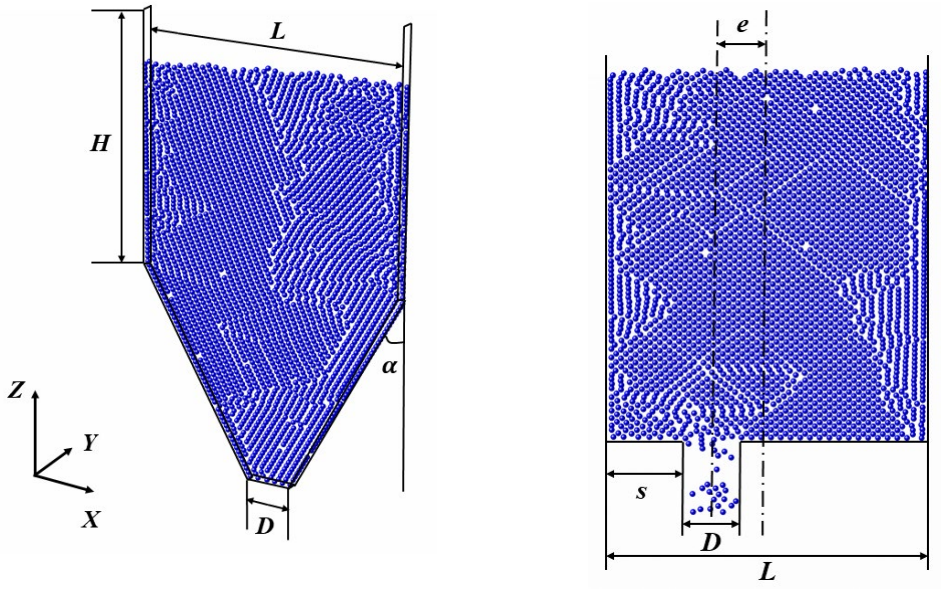

(a) (b)

Fig. 1 (a) Computational region for a 2D rectangular cross-section hopper ($\phi_B = 0.59$). (b) Schematic diagram of the eccentric hopper ($\phi_B = 0.57$).

According to the analysis of the flow rate, three states can be observed: increasing, steady and decreasing states, as presented in Fig. 2 (a). When the simulation starts, the granular materials flow rapidly and then reach a stable value with fluctuations. Following some calculation time, the flow decreases correspondingly as the hopper gets almost empty. We calculate the discharge rate W by time-averaging the instantaneous flow rate during the steady state and then compare it with the flow rate predicted by Beverloo's law for different orifice sizes, as displayed in Fig. 2 (b). $W^{2/3}$ depicts a linear relationship between flow rate and orifice size for multiple hopper angles in 2D.

The slope of the fitted curve and the intercept in the x-axis corresponds to C and kd, yielding C=0.58 and k=1.55. The value of k is close to the 1.7 predicted by numerical simulations of Anand et al. [15–17] and 1.5 obtained from experiments of Nedderman and Laohakul [38], where both hoppers are rectangular geometry. These data indicate that the simulation results are consistent with the predicted results and still follow Beverloo's law for 2D. In addition, the flow rate obtained from the DEM simulations for $\alpha = 90^{\circ}$ is accordant with the results of experiments we have carried out as a complement (see detail in supplementary file). As a result, the present DEM model is capable of recovering realistic flow rate of particles in a 2D hopper.

Table 1 Parameters used in the simulations.

Particle phase	
Particle number, N	3000
Particle diameter, d	3 mm
Particle density, ρ_p	2500 kg/m^3
Poisson's ratio, ν	0.25
Shear modulus, G	1×10^8 Pa
Interaction parameters	
Particle-particle	
Sliding coefficient, $\mu_{p,p}$	0.5
Rolling friction coefficient, $\mu_{rp,p}$	0.01
Restitution, $e_{p,p}$	0.2
Particle-wall	
Sliding coefficient, $\mu_{p,w}$	0.5
Rolling friction coefficient, $\mu_{rp,w}$	0.01
Restitution coefficient, $e_{p,w}$	0.2
Hopper geometry	
Width, L	100 mm
Orifice size, D	18, 30, 45, 60 mm
Thickness, Z	3.03 mm
Angle, α	15°, 30°, 55°, 75°, 90°
Eccentricity, s	0, 6, 12, 18, 24, 30 mm

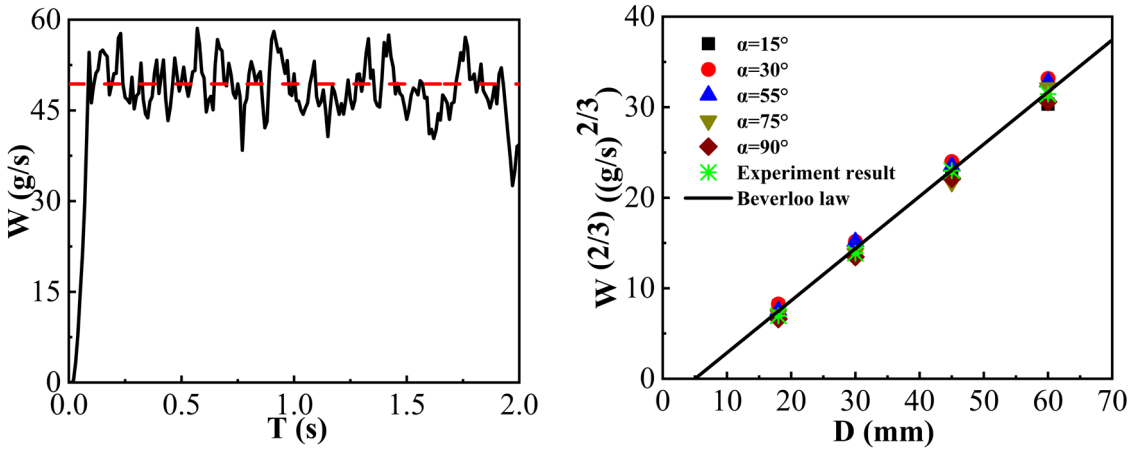

(a) (b)

Fig. 2 (a) The evolution of the instantaneous mass flow rate *versus* time. The dashed line indicates the mean value of the flow rate ($D/d = 10$, $\alpha = 90^{\circ}$). (b) Mass discharge rate per unit length raised to the $2/3$ power plotted as a function of the outlet width D for different hopper angles. The parameters of fitted line $C = 0.58$ and $k = 1.55$ are derived from Eq. (1).

4. Simulation results

4.1 The role of hopper angle

4.1.1 The effect of hopper angle on velocity profiles

The vertical velocity profiles for different hopper angles are presented in Fig. 3 (a)-(d). The vertical component v of the particle velocity is recorded as the particle passes through the aperture, the origin of the horizontal axis corresponds to the center of the hopper outlet. The velocity profiles exhibit parabolic behavior and depend on the outlet size. For a given hopper angle, the rise in D/d causes a decrease in the number of particle collisions, which results in faster particle velocities at the center and edge of the hopper exit. However, the particle velocity corresponding to the same D/d spikes with decreasing hopper angle when α is less than 55° since the hopper angle can reduce the particle stagnation zone. In addition, the velocity profiles are parabolic rather than hemispherical, as previously reported in Ref. [22], which agrees well with the experimental investigation of Janda *et al* [39].

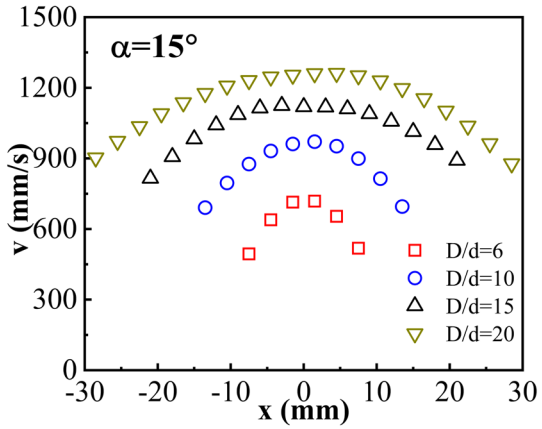
α=15°
v (mm/s)
x (mm)
D/d=6
D/d=10
D/d=15
D/d=20

(a)

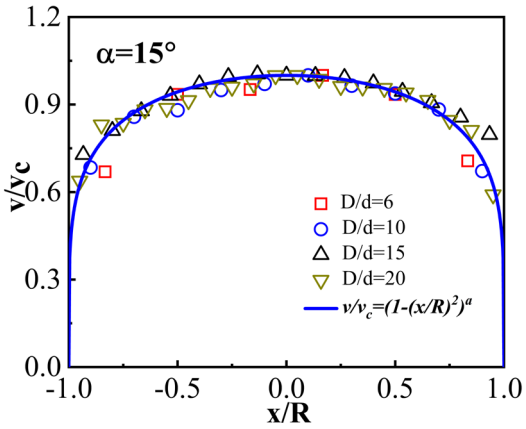
α=15°
v/vc
x/R
D/d=6
D/d=10
D/d=15
D/d=20
v/vc=(1-(x/R)2)a

(e)

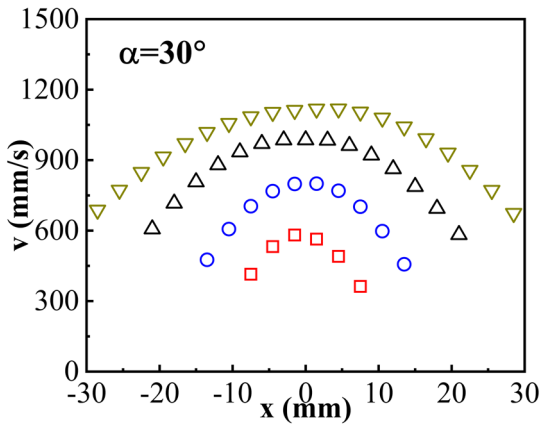
α=30°
v (mm/s)
x (mm)

(b)

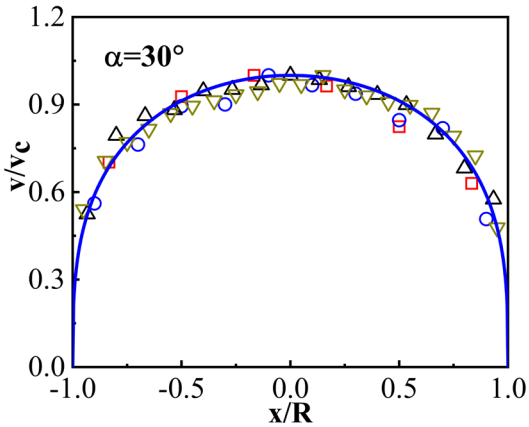
α=30°
v/vc
x/R

(f)

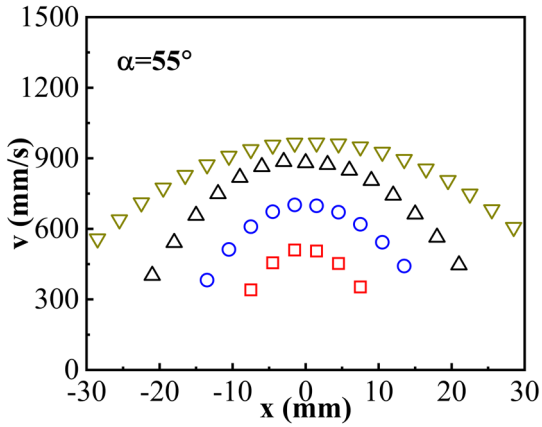
α=55°
v (mm/s)
x (mm)

(c)

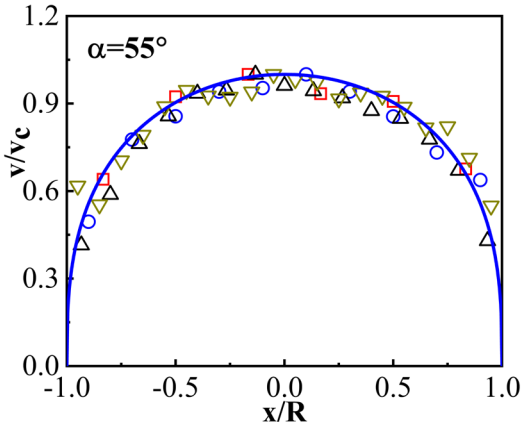
α=55°
v/vc
x/R

(g)

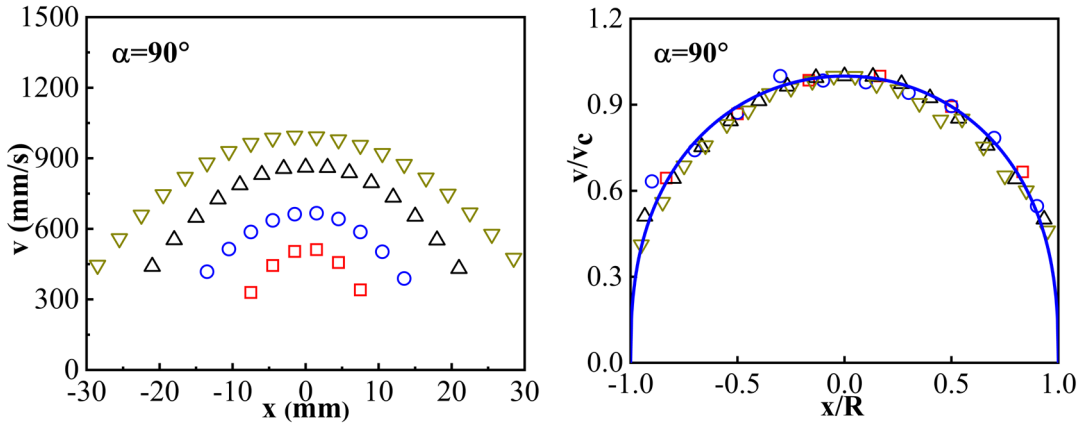

(d) (h)

Fig. 3 Velocity profiles with different outlet sizes for (a) $\alpha = 15^{\circ}$, (b) $\alpha = 30^{\circ}$, (c) $\alpha = 55^{\circ}$, and (d) $\alpha = 90^{\circ}$. Normalized velocities for different hopper angles: (e) $\alpha = 15^{\circ}$, (f) $\alpha = 30^{\circ}$, (g) $\alpha = 55^{\circ}$, and (h) $\alpha = 90^{\circ}$. v_c is the velocity of the particle at the center of the outlet when particles discharge from the hopper orifice. The solid lines represent the scaling functions.

Based on the bell-shaped feature of the velocity profiles (see Fig.3(a)-(d)), we use v_c measured at the center to normalize particle velocity corresponding to different outlet sizes and then plot them as a function of the dimensionless horizontal position x divided by aperture size R (R=D/2) (see Fig. 3(e)-(h)). The normalized velocity distributions in all cases collapse into a single curve, and this feature appears to show self-similar properties. As shown in Fig. 3(e)-(h), the hopper angle only slightly alters the curvature and magnitude of the velocity profiles. For the same hopper angle, the evolution of v_c with aperture size shows a linear relation with $\sqrt{R}$ with a slope that decreases with α, as presented in Fig. 4. When the hopper angles are 55°, 75° and 90°, the values of v_c for the same outlet are quite similar. Consistently with experimental study of Janda *et al.* [39], the expression $v_c = \sqrt{2g\gamma R}$ that suggests a free fall from a parabolic dome of radius γR. Regarding now the shape of the velocity profile, a simple expression can be proposed mixing parabolic and power-law relations:

$$v = v_c(1 - (x/R)^2)^a \quad (10)$$

where a is a fitting coefficient that controls the curvature of the velocity profile. The formula gives a good representation of the particle velocity profiles.

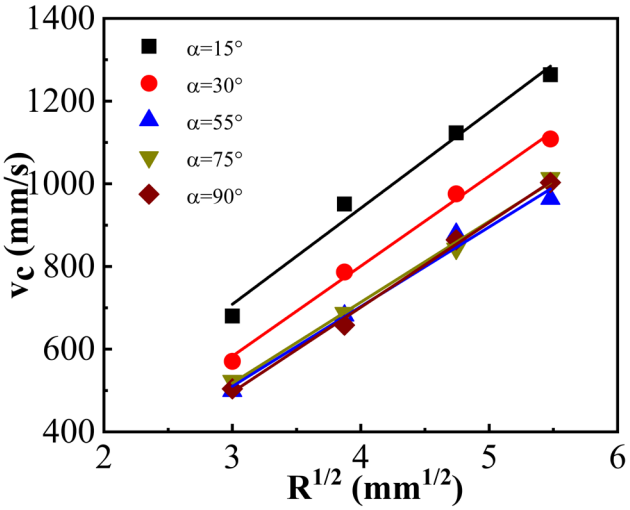

Fig. 4 Particle velocity v_c at the center of the outlet *versus* $\sqrt{R}$. The solid lines are fitted with $v_c = \sqrt{2g\gamma R}$, and the values of γ are shown in Table 2.

Fig.5 and Table 2 shows the correspondence between the values of a, γ and the hopper angle α. The exponent $a = 0.39$ in the normalized velocity profile with an angle of 90° is similar to the value of 0.38 derived by Zhou *et al*. [40] and 0.35 by Mendez *et al*. [10] for two-dimensional simulations, but slightly smaller than the experimental results 0.5 of Janda *et al*. [39] and Darias *et al* [16]. When $\alpha \geq 55^{\circ}$, the values of a are quite close and lead to a similar velocity profile (see Fig. 3(g)-(h)). The value of $\gamma = 1.66$ for 90° is greater than the 1.2 derived by Mendez *et al*. [10] and the 1.07 derived by Janda *et al* [39]. The value of γ at each hopper angle implies that the hopper angle controls the effective acceleration of the particles in the vertical direction. Thus, when the hopper angle decreases, the area where the particles stay on both sides of the bottom of the hopper shrinks, causing the particles to gather toward the orifice, which in turn leads to an overall increase in velocity.

Table 2 Values of fitting coefficients for velocity and volume fraction profiles.

α	a	γ	b	ϕ_∞
15°	0.20	2.81	0.16	0.79
30°	0.32	2.08	0.19	0.79
55°	0.35	1.61	0.30	0.78
75°	0.33	1.64	0.38	0.78
90°	0.39	1.66	0.39	0.78

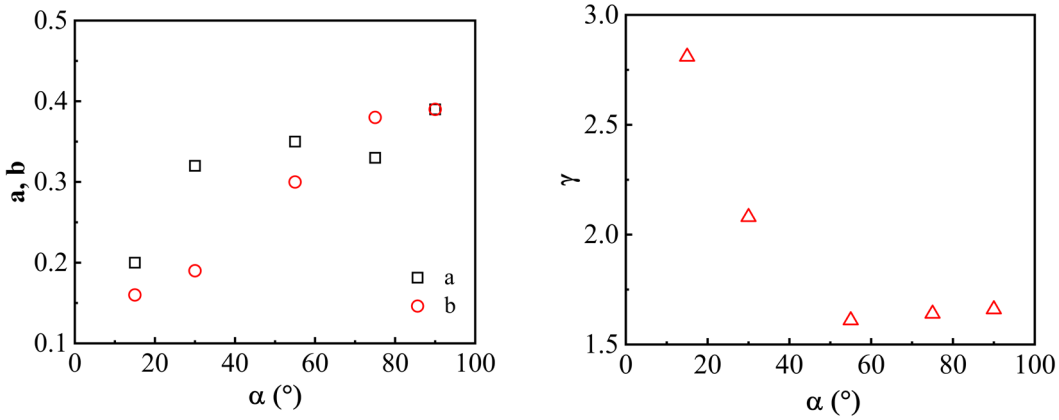

(a) (b)

Fig. 5 (a) Exponents a and b from velocity and volume fraction profiles, respectively, as a function of hopper angle α. (b) Corresponding fitting parameter γ with α.

4.1.2 The effect of hopper angle on volume fraction profiles

Regarding the relationship between particle volume fraction and hopper angle, Fig. 6 (a)-(d) displays the distribution of the volume fraction of particles along the outlet for different hopper angles. The profiles are bell-shaped with a curvature controlled by related the hopper angle. The outcomes reveal that the average value of the volume fraction decreases with decreasing outlet size for a fixed hopper angle, which is consistent with the results reported in the experimental and numerical investigations [16,39–41]. This observation can be explained by the case of granular flow through a small orifice in which intermittent flow or clogging probably occurs. Considerable dilatancy is normally required to prevent the formation of arches and ensure the flow of granular material across the orifice, particularly for $\alpha = 90^\circ$. In contrast, for a more

steeply inclined outlet, especially for $\alpha = 15^{\circ}$, it is easier to mobilise the granular material and furthermore to reduce the possibility of an arch interrupting the flow.

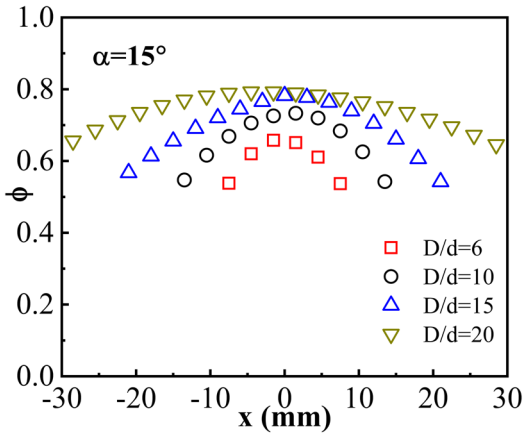

(a)

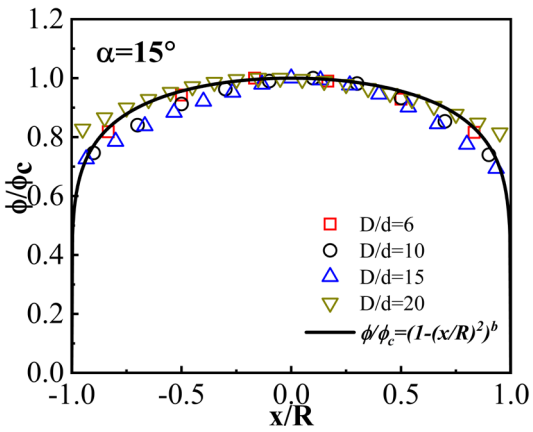

(e)

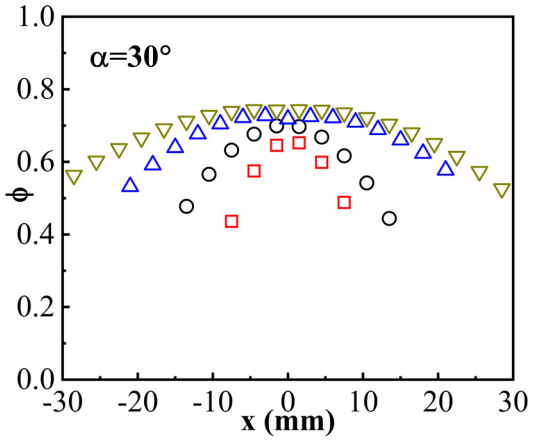

(b)

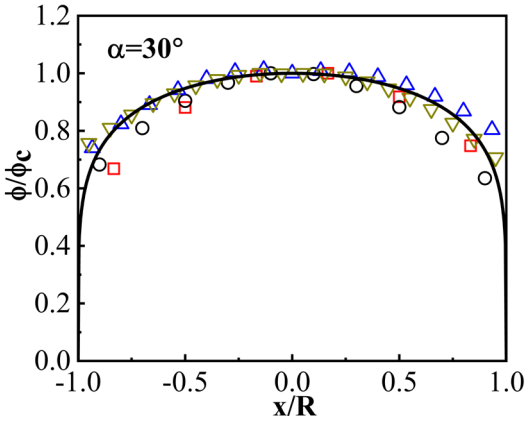

(f)

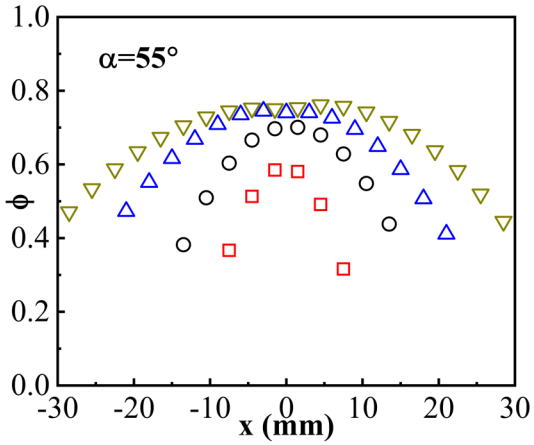

(c)

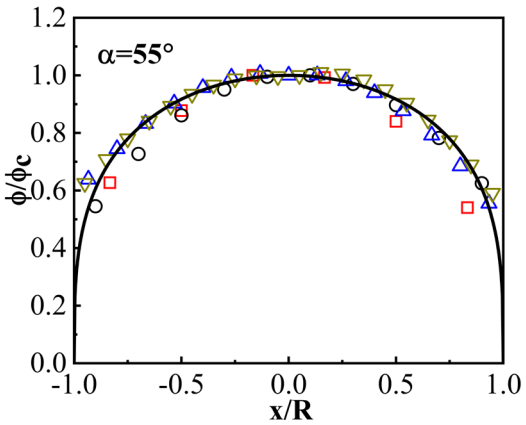

(g)

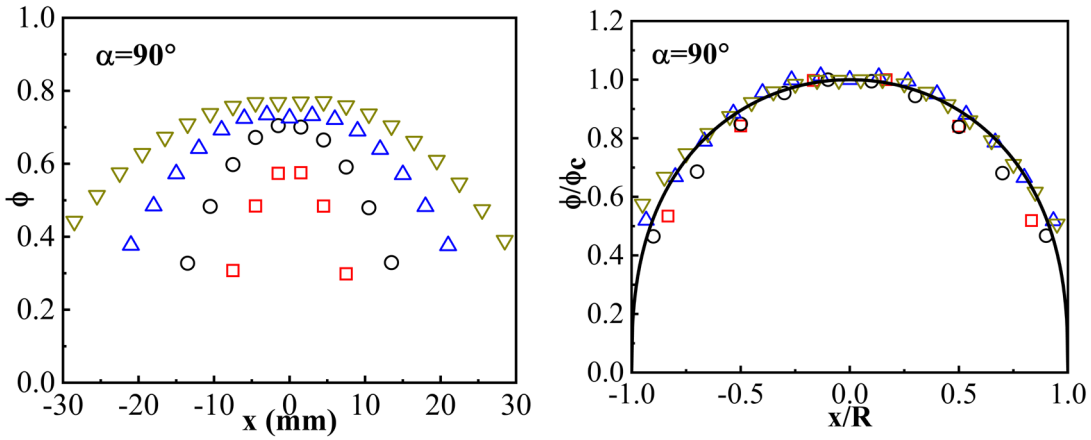

(d) (h)

Fig. 6 Distributions of the volume fraction of discharging particles at the outlet. (a) $\alpha = 15^{\circ}$, (b) $\alpha = 30^{\circ}$, (c) $\alpha = 55^{\circ}$ and (d) $\alpha = 90^{\circ}$. Profiles of the volume fraction normalized by ϕ_c for (e) $\alpha = 15^{\circ}$, (f) $\alpha = 30^{\circ}$, (g) $\alpha = 55^{\circ}$, and (h) $\alpha = 90^{\circ}$. The solid line is the fitting function (Eq. (11)).

To confirm the self-similarity of the profiles, these are rescaled by the volume fraction at the center of the outlet ϕ_c, as presented in Fig. 6(e)-(h). As expected, all the profiles collapse into a single curve, and self-similar features are thus obtained. Following the previous analysis, the profiles can be fitted conveniently by the same type of mixed parabolic and power law:

$$\phi = \phi_c(1 - (x/R)^2)^b \tag{11}$$

where b is a fitting parameter that determines the shape of the volume fraction profile. Fitting with this formula, we obtain the value of the parameter b that gives the best fit for each hopper angle (see Table 2 and Fig.5a). And its value is close to a, showing similar curvature for both velocity and solid fraction profiles. We discover that b increases as the hopper angle rises. Although the index $b = 0.39$ for 90° is larger than the reported 0.19 derived by Zhou *et al*. [40] , 0.16 by Mendez *et al*. [10] and 0.22 of Janda *et al*. [39], this higher value is probably due to the transformation from 3D to quasi-2D silos which the thickness of the front-back wall (Z) and the wall-particle friction coefficient ($\mu_{p,w}$) have significant influence on distribution of the volume fraction [42].The profiles still remain self-similarity for the wall-particle less friction $\mu_{p,w} = 0.01$ (Fig.S2(a)) and for different confinement thickness (Fig.S2(b)). The flow rate W decreases when increasing the wall-particle fiction coefficient (see Fig.S3(a)) or

the confinement thickness (Fig.S3(b)). Then a value of index $b = 0.2$ for the wall-particle less friction is obtained as displayed in Fig.S4, which is close to the references [10,39,40]. The current DEM model can better reproduce the experimental results by adjusting the parameters reasonably. In addition, the self-similarity of volume fraction strongly indicates that the motion of the granular material crossing the outlet is not sensitive to the onset of clogging.

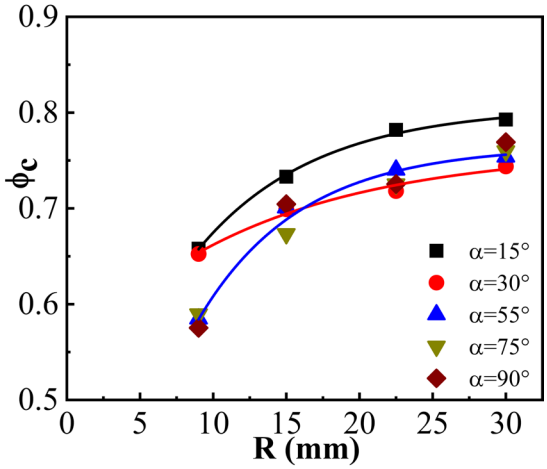

Fig. 7 2D volume fraction in the center of the orifice ϕ_c *versus* R. The relationship between ϕ_c and R is fitted by Eq. (12), where the black line is hopper angle $\alpha = 15^{\circ}$, the red line corresponding to $\alpha = 30^{\circ}$, and the blue line collects all the data for $\alpha = 55^{\circ}$, $\alpha = 75^{\circ}$, and $\alpha = 90^{\circ}$.

Regarding the volume fraction at the center of the rectangular hopper, Fig. 7 describes the relationship between ϕ_c and R obtained from Eq. (12). Based on previous studies [23,39], the following relationship can be fitted by:

$$\phi_c = \phi_\infty(1 - \tau_1 e^{-2\tau_2 R}) \tag{12}$$

where τ_1 and τ_2 are fitting parameters, the plot implies that ϕ_c increases with R for different hopper angles. This behavior can be attributed to the particle expansion of the materials when they pass through the small aperture. We calculate the maximum difference in the ϕ_c value, which is 12.5% for a small orifice $R = 9$ mm, and this gap reduces to 6.2% for $R = 30$ mm. Consequently, as the outlet becomes larger, the particle volume fraction tends to an asymptotic value ϕ_∞ that is listed in Table 2. This result is consistent with the outcome found in the experimental work [16]. Combining all the values of ϕ_∞ shows that the volume fraction of granular material crossing

through the orifice is always less than the bulk density. In addition, to maintain the flowability condition for granular material, ϕ_∞ is slightly smaller than the critical value for jamming.

4.1.3 Flow rate of a rectangle hopper with different angles

To predict the flow rate from a rectangular hopper, we calculate the mass flow rate W using the particle velocity and volume fraction described in the previous section. To better understand the physical meaning behind the particle flow, the mass flow density $\vec{q}$ is introduced as follows [24]:

$$\vec{q} = \frac{2}{3}\overrightarrow{e_z}\rho_p\phi(x,z)v(x,z) \tag{13}$$

where $v(x,z)$ and $\phi(x,z)$ correspond to Eq. (10) and (11) in a 2D rectangular hopper, and $\frac{2}{3}\phi(x,z)$ is the volumetric fraction corresponding to a mono-layer of spheres with a 2D solid-fraction. Substituting $v_c = \sqrt{2g\gamma R}$ into Eq.(13), a novel formula is obtained to describe the mass flow rate from a 2D rectangular hopper:

$$W = \int \vec{q}(x,z=0)\cdot\vec{d}A = \frac{2}{3}\phi_\infty v_c \int_{-r}^{r}\int_{-R}^{R}\left(1-\left(\frac{x}{R}\right)^2\right)^{a+b} dxdz = \frac{2\sqrt{2}}{3}\beta\left(\frac{1}{2}, 1+[a+b]\right)\rho_p\sqrt{\gamma g}\phi_\infty dR^{3/2} \tag{14}$$

All the parameters in Eq. (14) have clear physical meanings. The β function is related to the profile shape of the velocity and volume fraction. Note that this function simply leads to variation in the curvature profiles, which has a weak influence on the flow rate. While parameter γ controls the acceleration of the particle falling, it plays a critical role in the flow rate, especially when the hopper angle changes.

The flow rate W obtained from our simulations is compared with the prediction in Eq. (14) for different hopper angles in Fig. 8(a). A satisfactory agreement can be observed, although there is a small discrepancy for low value of R. The reason could be the fact that the prediction in Eq. (14) is calculated using ϕ_∞ instead of the accurate value. Since intermittent flow or clogging gives rise to fluctuations at a small orifice size, the method of calculating the flow rate adopts a volume fraction with a limited value corresponding to a sufficiently large orifice size. The impact of outlet size on the

maximum volume fraction is neglect. In addition, the volume fraction of particles for a large outlet is close to ϕ_∞. In the end, the flow rate in Eq. (14) is generally faster than the simulation results only for a small outlet.

From Eq. (14), the dimensionless discharge rate $W^{2/3}$ follows the expected linear growth with R, as shown in Fig. 8(b). An interesting finding is observed where the mass flow rates related to the hopper angle are quite similar at a fixed R for $55^\circ < \alpha < 90^\circ$. For a hopper angle of less than 55°, the gap becomes pronounced at a large orifice size. A large R leads to an increase in the particle velocity and volume fraction as described above, which results in a faster flow. When the hopper angle α is constant, the mass flow rate of the hopper increases with the growth of the outlet size. It is worth noting that the slope of each line gives the Beverloo parameter $C(\alpha)$ in Eq. (1), whose value is dependent on hopper angle when $\alpha < 55^\circ (C(15^\circ) = 0.72, C(30^\circ) = 0.65)$. As $\alpha > 55^\circ$, the fitting parameter reaches a constant value around 0.55 and is not sensitive to the hopper angle anymore.

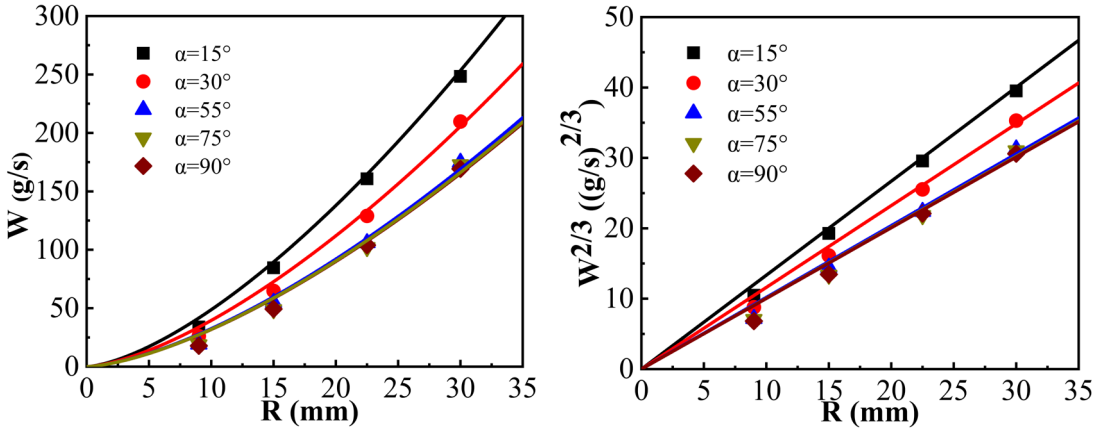

(a) (b)

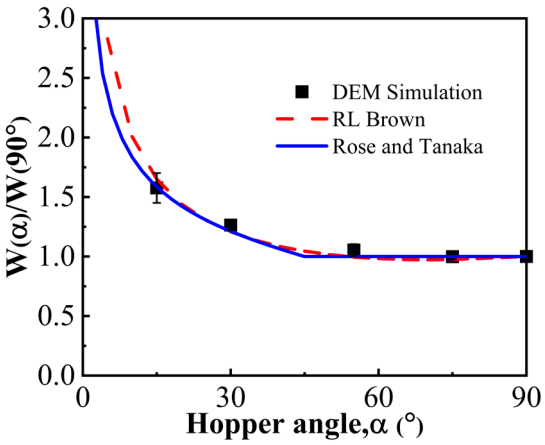

(c)

Fig. 8 (a) Mass flow rate for different hopper angles. (b) The flow rate raised to the $2/3$ power as a function of R. The continuous lines in both graphs correspond to Eq. (14) and its scaling function with the fitting parameters obtained in Table 2. (c) Flow rates of particles normalized by the prediction for a hopper with a flat bottom.

To reveal the role of the rectangular hopper angle more intuitively, we use the mass flow rate with a flat-bottom outlet ($\alpha = 90^{\circ}$) to normalize W at various hopper angles. Fig. 8 (c) displays the normalized flow rate obtained from the present DEM simulations, together with the results of Rose and Tanaka [43] , and Brown [22] (Eq. (3)). A close agreement is obtained regarding the relationship between the hopper angle and the mass flow rate ratio. Though there is a discrepancy observed among the dispersion points, the maximum deviation is only 4.6% at $\alpha = 55^{\circ}$.

Finally, the coefficients included in Eq. (14) give a clear physical interpretation: the symmetry of the profiles associated with the hopper angle is reflected by the β function as the grains close to the orifice undergo shear expansion and γ controls flow acceleration.

4.2 Influence of the eccentric position of the outlet

Apart from the hopper angles, the location of the outlet also influences the granular discharge flow. In the present simulations, two parameters are used to define the location of the outlet, as presented in Fig. 1(b). The first one is given by e, which represents the distance between outlet center and hopper central axis. The second one, measured by s, denotes the gap between the left corner of the outlet and the left wall. Note that $e + s = (L - D)/2$. The influences of e and s on hopper flow could result

in comparatively different physical conditions for extreme eccentricity, which can be analyzed in terms of the velocity vector. Thus, Fig. 9 displays two different flow patterns where the particles discharge from the outlet at both sides (Fig. 9(a)) and, imposed by s=0, another one only from one side (Fig. 9(b) and (c)). Visualizing particle movements using velocity vectors also shows the way in which the granular medium is self-organizing within the main flow zone, which extends laterally across the width of the opening, and outside it. For the smaller orifice size (Fig. 9(a) and (c)), the discharge main zone contains recirculation cells, whereas, for the larger orifice size (Fig. 9(b)), there is a vertical flow in which the velocity vectors are all aligned. Particularly noticeable in Fig. 9 (a) and (c), the area outside the main flow is ordered according to a typical monodisperse 2D-granular packing pattern. Thus, in analogy, a similar flow state is obtained for all cases when the outlet is close to the sidewall. This finding indicates that s can better characterize the eccentric location of outlets, which is consistent with a recent study reported by Ashish Bhateja *et al*. [23].

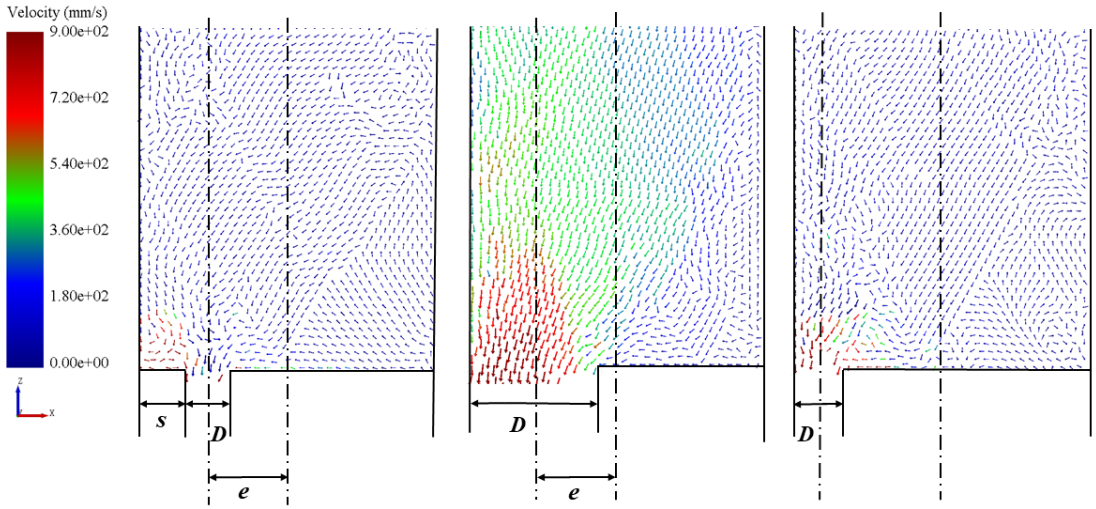

(a) e=27mm, D/d=6 **(b) e=27mm, s=0mm, D/d=15** **(c) s=0mm, D/d=6**

Fig. 9 The particle velocity vector obtained from at moments during the simulation of particle flow in a hopper with an eccentric outlet.

4.2.1 Velocity profiles through outlets at eccentric locations

Following the previous analytical approach, the velocity profiles through the eccentrically located outlet are displayed in Fig. 10 (a)-(d). Concerning the case of the

outlet from the center ($s = 24$ mm) to the hopper wall ($s = 0$), the asymmetry behavior in the velocity profiles gradually becomes obvious in Fig. 10 (a)-(d), where parameter s is the eccentricity of the location of the outlet and $x^* = (x - e)/R$ is the dimensionless horizontal distance from the outlet axis. This behavior tends to disappear as s increases due to the outlet being close to the center.

To test the self-similarity of the velocity profiles, we can first consider the previous scaling where the velocity is scaled by $\sqrt{2gR}$ instead of v_c as follows:

$$\bar{v} = v/\sqrt{2gR} = \varepsilon_{\mathrm{e}}(1 - x^{*2})^{\sigma_e} \tag{15}$$

where the ε_{e} and σ_e are fitting parameters. Note that e=0 corresponds to the previous study case where the outlet is located at the center. Consistently, the same exponent and proportionality factor are obtained: $\sigma_{e=0} = a$ and $\varepsilon_{\mathrm{e}=0} = \sqrt{\gamma}$. Fig. 10(e)-(h) shows the velocity profiles scaled by $\sqrt{2gR}$ collapse into the same fitting curve. The velocity corresponding to the eccentric location of the outlet is obviously faster for $s = 0$ than the other cases. This finding indicates that the location of the outlet can be regarded as a switch for controlling the particle flow rate. Furthermore, the normalized velocity profiles remain self-similar for all values of s, as displayed in Fig. 10(e)-(h). Such scaling characteristic for the most extreme off-centred outlet ($s = 0$) is encouraging, and it provides feasibility to expand the self-similar profiles from the centric outlet to the border outlet in the hopper flow. Generally, this discovery gives a unified understanding of granular flow by combining the scaled velocity profiles at the centred and border outlets.

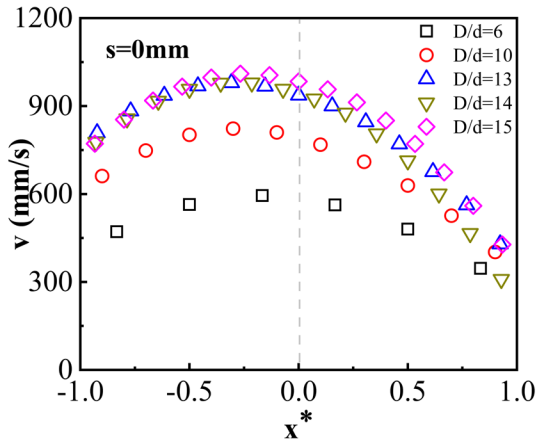
s=0mm
D/d=6
D/d=10
D/d=13
D/d=14
D/d=15
v (mm/s)
x*

(a)

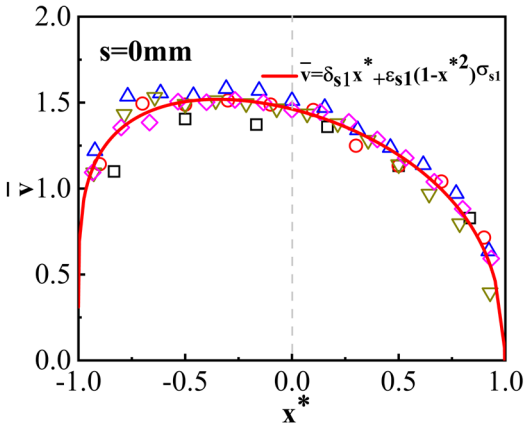
s=0mm
$\bar{v}=\delta_{s1}x^{*}+\varepsilon_{s1}(1-x^{*2})\sigma_{s1}$
x*

(e)

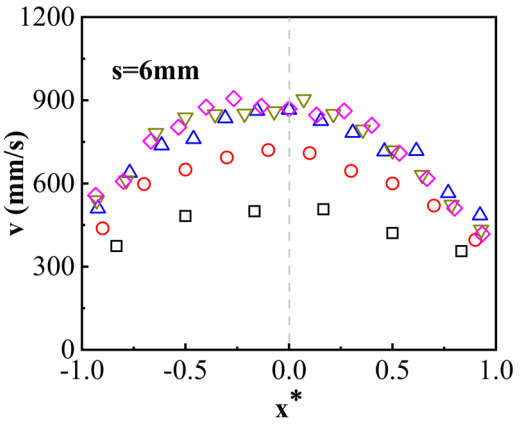
s=6mm
v (mm/s)
x*

(b)

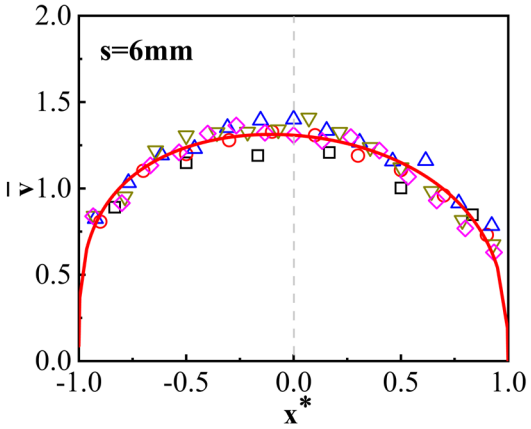
s=6mm
x*

(f)

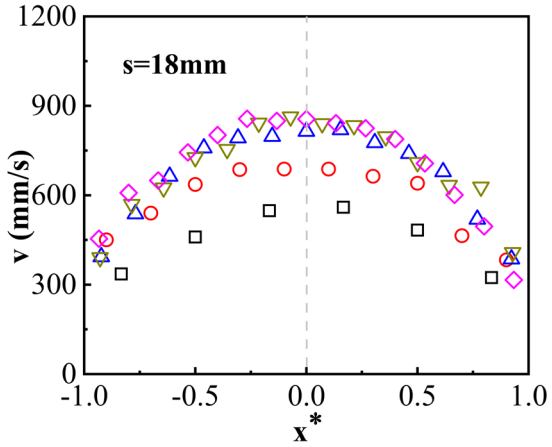
s=18mm
v (mm/s)
x*

(c)

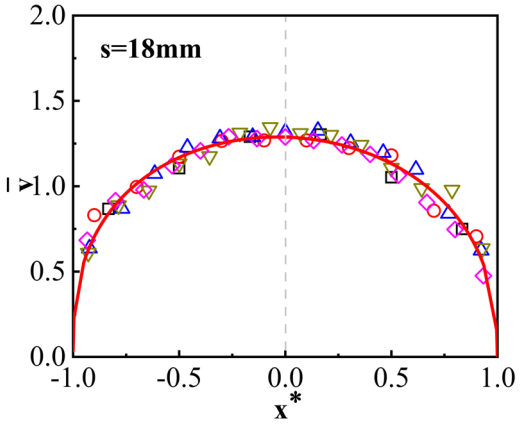
s=18mm
x*

(g)

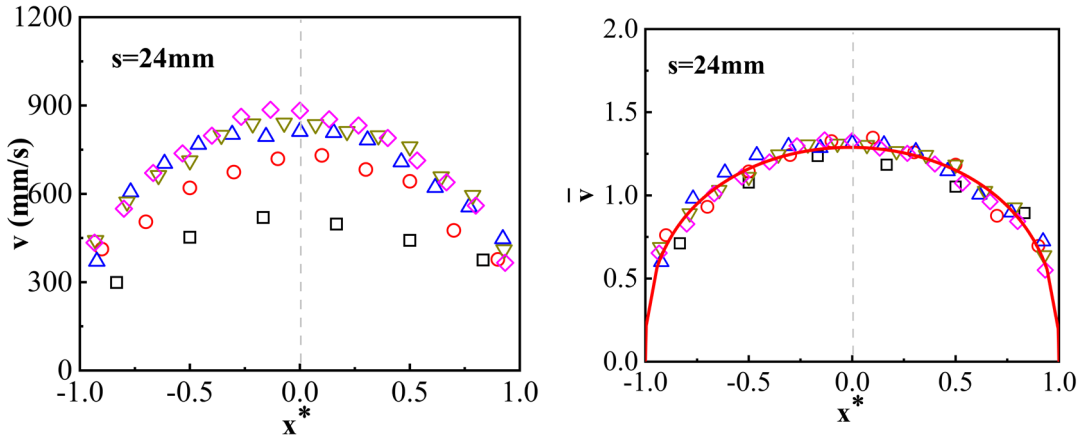

(d) (h)

Fig. 10 Velocity profiles for different outlet sizes where (a) $s = 0$, (b) $s = 6$ mm, (c) $s = 18$ mm, and (d) $s = 24$ mm. The normalized velocity profiles at the hopper exit are (e) $s = 0$, (f) $s = 6$ mm, (g) $s = 18$ mm, and (h) $s = 24$ mm. The red solid line for (e)-(h) is obtained from Eq. (16).

The dimensionless values of the velocity profiles in Fig. 10(e)-(h) are in full agreement with the discrete velocity points. Note that the Eq. (15) in the form $\varepsilon_e(1 - x^{*2})^{\sigma_e}$ is only valid to fit the collapse data for the case where the outlet is close to the center. The profile presents dissymmetry characteristics for the extreme eccentricity (s=0), which cannot be fitted by Eq. (15) obtained from the self-similarity analysis. To account for the dissymmetry of the profiles controlled by the parameter s, we propose here a unified equation:

$$\bar{v} = \delta_{s1} x^* + \varepsilon_{s1}\left(1 - x^{*2}\right)^{\sigma_{s1}} \tag{16}$$

which is an adapted version of formula (15), the average value of the parameter $\varepsilon_{s1} = 1.3$ is found to satisfactorily fit the solid lines in Fig. 10(e)-(h). The parameter δ_{s1} regulates the normalization of the eccentric velocity, and σ_{s1} determines the smoothness of the normalized velocity profile. The additive term $\delta_{s1} x^*$ models the asymmetry of the velocity profile. Parameter δ_{s1} is related to s, as shown in Fig. 11(a) dimensionless excentricity $s^* = 2s/(L - D)$ to comprehensively consider the role of L and D. When the hopper outlet moves from the border ($s^* = 0$) to the center, the value $\delta_{s1} x^*$ decreases, and the asymmetric behavior of the velocity profiles gradually

disappears. In such case, the value of δ_{s1} grows almost exponentially from a negative value until reaching 0 and the symmetry velocity profile is recovered, which is consistent with analysis of the self-similarity. Moreover, δ_{s1} also controls the shift position of the maximum particle velocity, ensuring that the velocity profile becomes more symmetrical with the increase of s^*. Besides, the form of the Eq. (16) is accord with the one reported by a recent work of Bhateja *et al* [23]. Thus, the term $\varepsilon_{s1}\left(1-x^{*2}\right)^{\sigma_{s1}}$ keeps the self-similarity and $\delta_{s1}x^*$ controls the asymmetry in Eq. (16) can be well fitted the velocity profiles for eccentrically located outlets.

Regarding the exponent σ_{s1} in Eq. (16), it is related to the shape of the velocity profile, which plays the role similar to the parameter a as discussed in the section of the hopper angle. As the outlet goes from the wall to the center, s^* gradually increases from 0 to 1, the original asymmetric particle velocity profile becomes more symmetrical, and its maximum particle velocity gradually returns to the center. Thus, the value of exponent σ_{s1} is related to s^* under the consideration of the outlet location. The variation in exponent σ_{s1} with s^* is presented in Fig. 11 (b). σ_{s1} increases exponentially reaching a constant for large s^*. A fitting function $\sigma_{s1} = 0.39 - 0.12e^{-3.74s^*}$ in Fig.11(b) is obtained. A large value of s^* leads to the term $e^{-3.74s^*}$approaching 0, the velocity profile index σ_{s1} increases exponentially to near 0.39 (centered hopper $s^* = 1$). The velocity profiles tend to become symmetric. Note that the role of σ_{s1} in dictating the profile shapes depends not only on the eccentricity s^* but also on the hopper angle, as reported in the previous section.

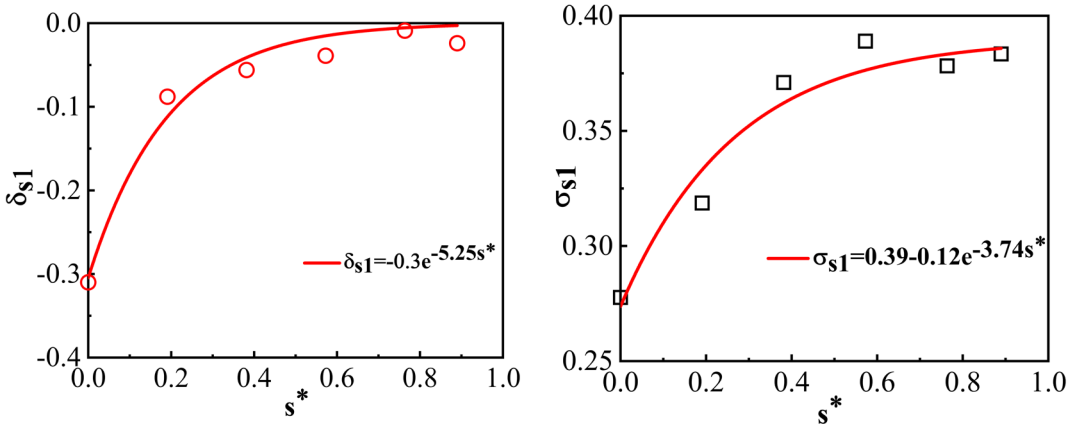

(a) (b)

Fig. 11 The relationship between parameters (a) δ_{s1} and (b) σ_{s1} and eccentricity.

4.2.2 Volume fraction profiles through eccentric location of outlets

Following the same procedure for particle velocity, Fig. 12 (a)-(d) presents the measured volume fraction profiles through the eccentrically located outlet characterized by parameter s. Fig. 12 (a) shows that the profiles through the extreme eccentrically located outlet ($s = 0$) clearly exhibit asymmetric behavior owing to prominent boundary influences. As s continues to increase, symmetric profiles with x^* for all the outlet sizes are gradually recovered. To verify the self-similar feature of the volume fraction profiles, all the data are normalized by the maximum value at the outlet ϕ_{max}. As expected, the points nicely collapse into a single fitting curve for the outlet at both the center and border (Fig.12 (e)-(h)), in line with previous studies [10].

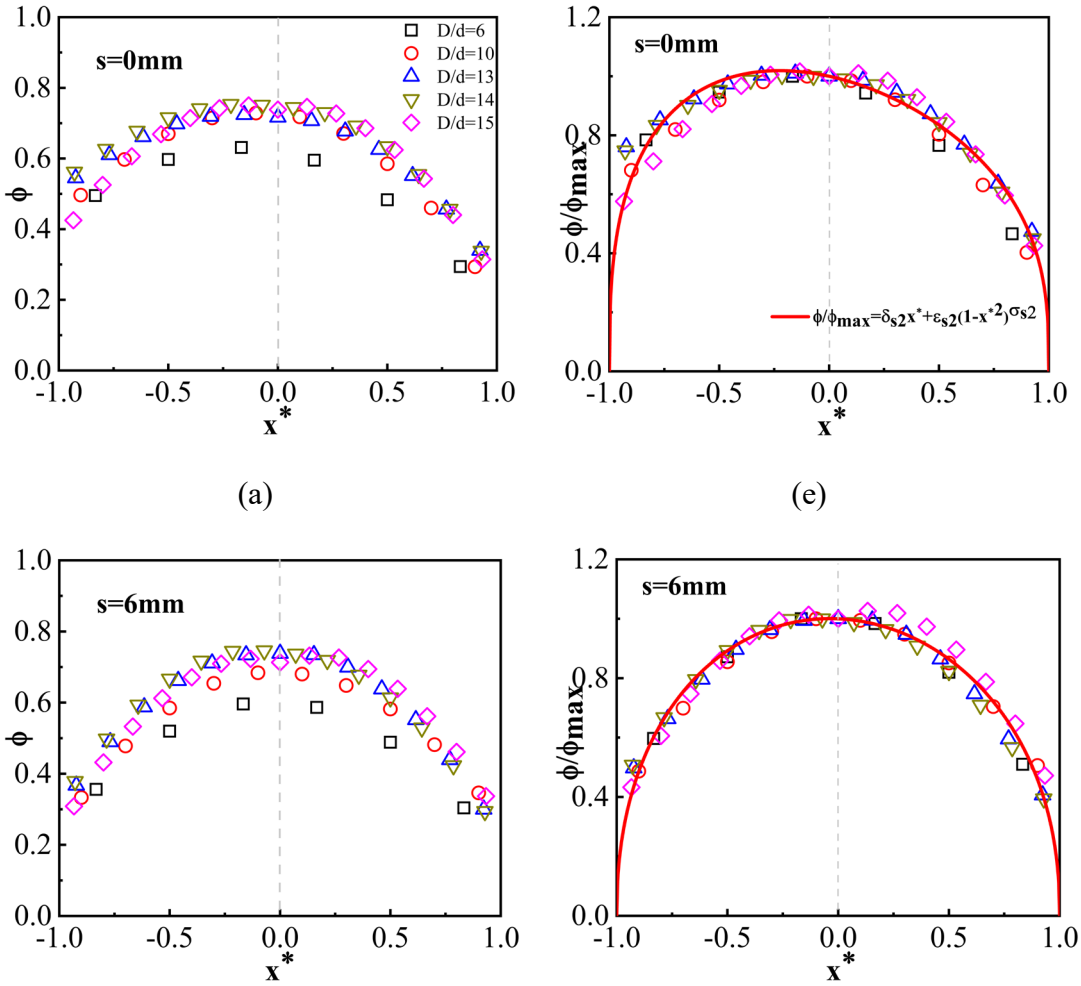

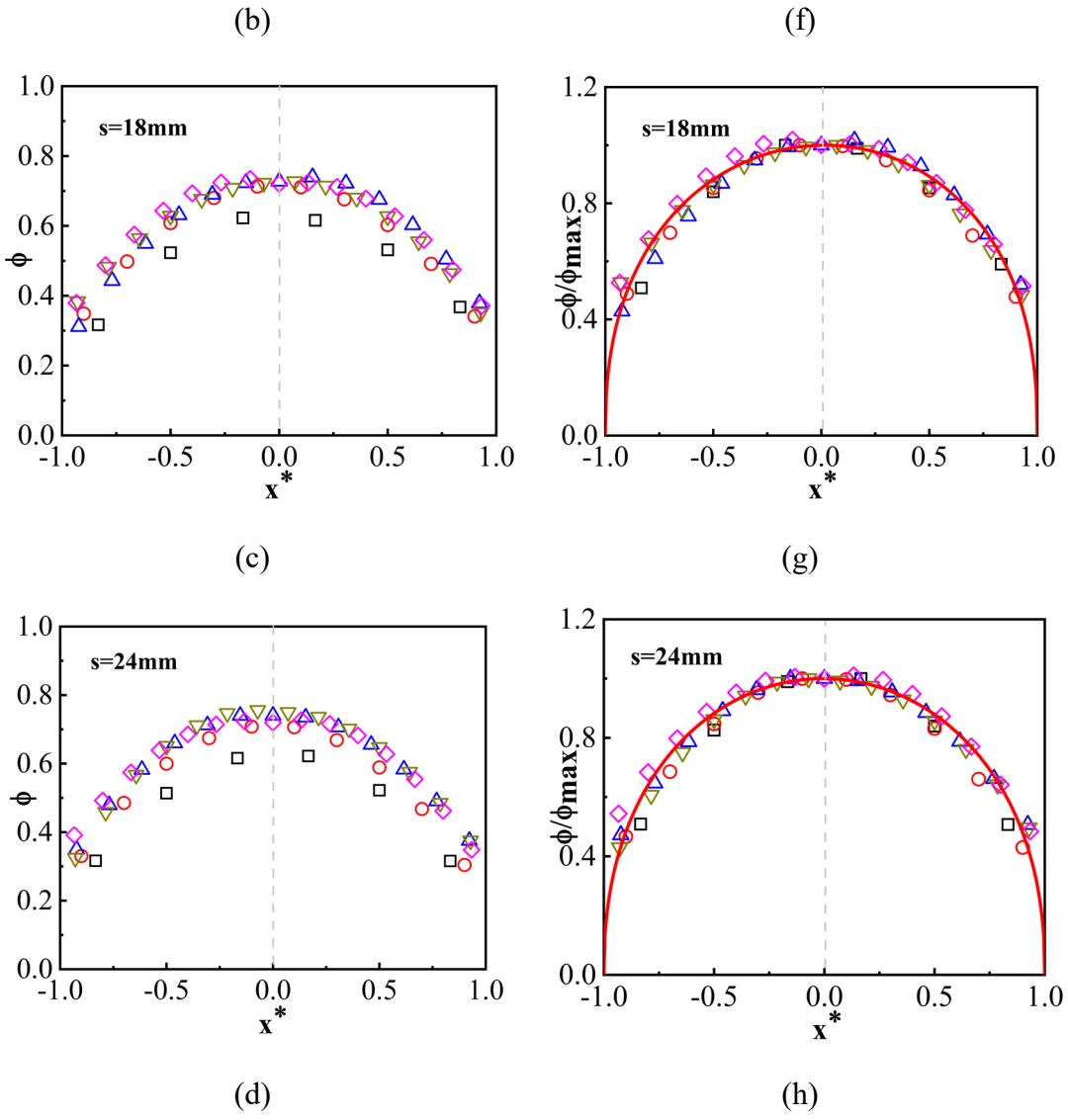

Fig. 12 Volume fraction profiles with different outlet sizes for (a) $s = 0$, (b) $s = 6$ mm, (c) $s = 18$ mm and (d) $s = 24$ mm. Corresponding in normalized volume fraction for (e) $s = 0$, (f) $s = 6$ mm, (g) $s = 18$ mm and (h) $s = 24$ mm.

Consistently with velocity scaling, the volume fraction profiles are approximated by the following expression:

$$\phi/\phi_{max} = \delta_{s2}x^* + \varepsilon_{s2}\left(1 - x^{*2}\right)^{\sigma_{s2}} \tag{17}$$

where δ_{s2} and ε_{s2} are the fitting parameters, and the value of the index σ_{s2} determines the profile shape. ϕ_{max} stands for the maximum volume fraction at the outlet. Fig. 13 presents the dependence of ϕ_{max} on R, and the relationship appears to be consistent with an exponential asymptotic increase. Moreover, the ϕ_{max} for s=6-30 mm share a common fitting curve except for the outlet close to the wall, the fitted

parameters in the curve $\tau_1 = 5.34$ and $\tau_2 = 0.19$ are obtained from Eq. (12). For the situation where $s = 0$, the maximum value of the volume fraction ϕ_{max} obtained at the hopper orifice is shifted toward the left side of the outlet, where the corresponding fitting parameters are $\tau_1 = 3.74$ and $\tau_2 = 0.18$.

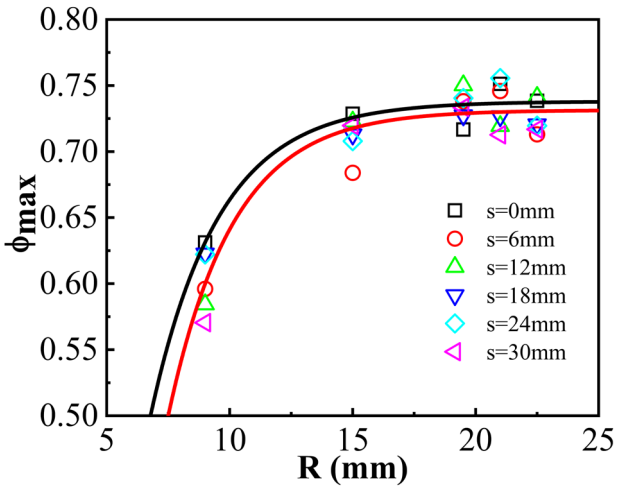

Fig. 13 Dependence of the maximum volume fraction ϕ_{max} at the outlet and R. The fitted curves are obtained from Eq. (12), where the black line stands for s = 0 and the red line is the remaining s values.

Both δ_{s2} and σ_{s2} can be described by specific formulas incorporating the eccentricity dimensionless parameter s^*, as displayed in Fig. 14. δ_{s2} accounts for the non-symmetric shape of volume fraction profiles. This term vanishes for large s^* where the outlet is back at the center of the hopper. The exponent σ_{s2} in Fig. 14(b) fluctuates approximately 0.42 when the eccentricity s is taken from 6 to 30 mm. In this range, the profiles in both velocity and volume fraction share almost the same curvature. However, σ_{s2} is smaller for $s^* = 0$ than other cases, which further demonstrates that the boundary wall indeed has an impact on the granular flow in the hopper with an eccentric location of the outlet. But this effect is limited as the value obtained for $s^* = 0.09$ has almost already reached the plateau.

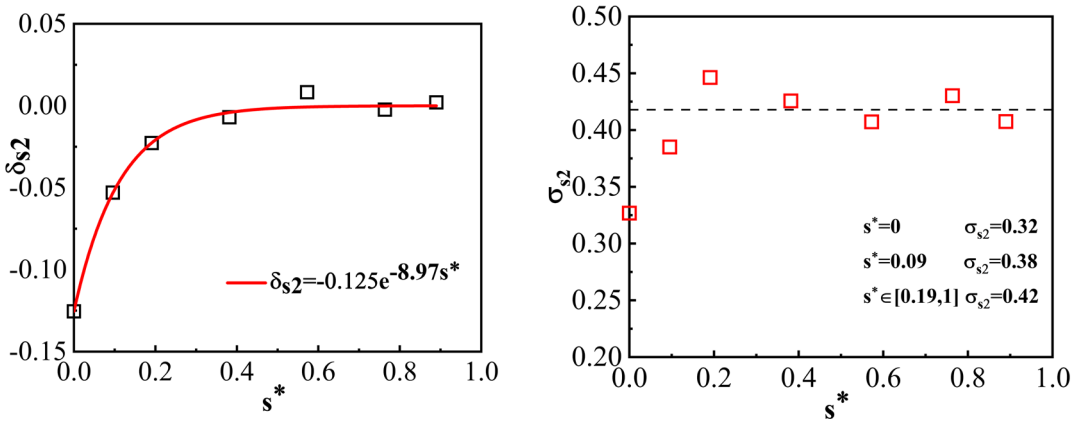

(a) (b)

Fig. 14 Variation in the parameters (a) δ_{s2} and (b) σ_{s2} with eccentric variable s^*.

4.2.3 Flow rate of a hopper with an eccentrically located outlet

To predict the flow rate of the rectangular hopper with an eccentric outlet location, we combine Eq. (13), (16) and (17) to yield:

$$W = \frac{2}{3}\left[\frac{2}{3}\delta_{s1}\delta_{s2} + \varepsilon_{s1}\varepsilon_{s2}\beta(1{,}1 + (\sigma_{s1} + \sigma_{s2}))\right]\rho_p\phi_{max}vdR \tag{18}$$

where the values of the parameters δ_{s1}, δ_{s2}, ε_{s1}, ε_{s2}, σ_{s1} and σ_{s2} are listed in Table 3. The parameters δ_{s1} and δ_{s2} cannot be negligible when s =0, but their values give no contribution for other s after integration.

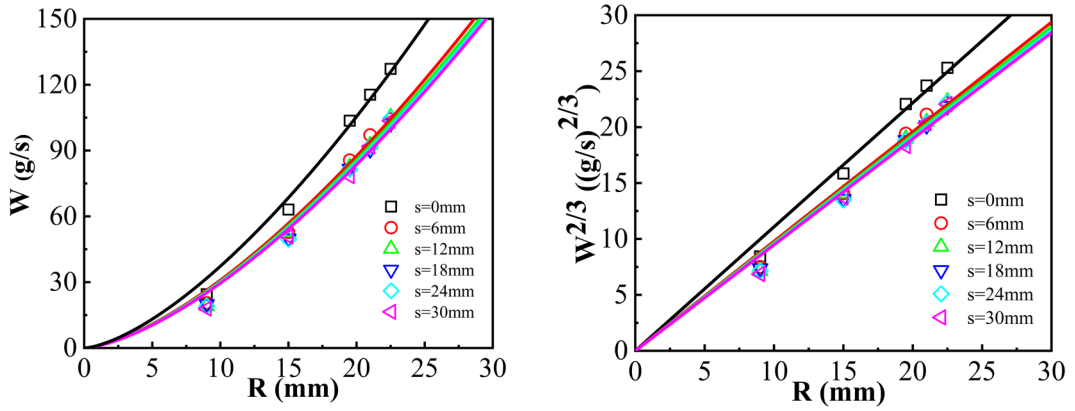

(a) (b)

Fig. 15 (a) Mass flow rate for different eccentricities s. (b) The flow rate raised to the $2/3$ power as a function of R. The continuous lines in both graphs correspond to Eq. (18) and the scaling function with the fitting parameters obtained in Table 3.

Table 3 Values of the fitting coefficients for the velocity and volume fraction curves.

s	δ_{s1}	δ_{s2}	ε_{s1}	ε_{s2}	σ_{s1}	σ_{s2}

0 mm	-0.31	-0.13	1.46	1	0.28	0.32
6 mm	-0.09	-0.02	1.3	1	0.32	0.44
12 mm	-0.06	-0.007	1.3	1	0.37	0.42
18 mm	-0.04	0.008	1.3	1	0.4	0.4
24 mm	-0.01	-0.002	1.3	1	0.38	0.43
30 mm	-0.02	0.002	1.3	1	0.38	0.41

Fig. 15(a) presents the comparison of the mass flow rate obtained by Eq. (18) and calculated from simulations. Good agreement is observed for all s. The flow rates of the hoppers for $s = 0$ are larger than those of other eccentric cases in the sense that the presence of the boundary slip velocity and the wall effect enhance the flow rate of particles. Fig. 15(b) linearizes the flow rate to a power 3/2 with respect to R, the outlet located at the wall produces higher flow rate than other cases, and the trend is still linear. Note that Beverloo law in Eq. (1) derives $C(s = 0) = 0.6$ higher than $C(s \neq 0) = 0.52$ from two different slopes of the fitting line.

The mass flow rate made dimensionless by W_0 *versus* s^* is plotted as depicted in Fig. 16, where W_0 corresponds to the flow rate of the hopper without eccentricity (i.e., for $e = 0$ and each D/d ratio). At $s^* = 0$, the mass flow rate of the hopper is 1.2-1.4 times larger than that of the non-eccentric outlet. In the range of 0.2< s^*<1.0, the flow rate of the hopper is nearly identical to that of the non-eccentric hopper. For a given eccentricity s^*, the hopper with a smaller outlet provides larger flow increments. Thus, this finding can provide a guideline for designing a hopper with an appropriate outlet location to control the flow rate. As reported in experimental work [7–10] where the outlet is at the lateral wall and the flow is increased.

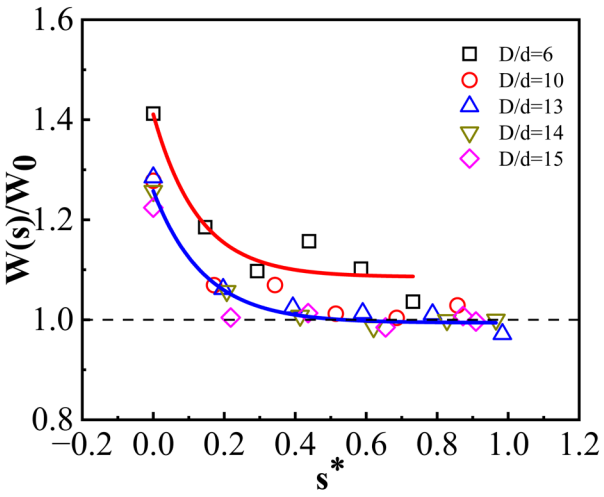

Fig. 16 Normalized flow rate *versus* eccentricity s^* for different hopper outlets.

5. Conclusions

In this paper, we numerically study the physical modeling of the granular discharge process. An 2D extensive DEM parametric study was carried out to investigate the influence of the rectangular hopper angle and eccentricity on the particle flow.

Self-similar properties for velocity and volume fraction profiles were observed for all hopper angles, which is in satisfactory agreement with the experimental results of Mendez *et al*. [10], Darias *et al*. [16] and Janda *et al*. [39]. An adapted expression for predicting the mass flow rate by taking into account the hopper angle was given in terms of the scaled velocity and volume fraction. All fitting coefficients have clear physical meaning. The parameter a implied in the velocity profiles determines the smoothness of the outline. In the particle volume fraction profiles, b controls the flatness of the profiles.

In the case of a hopper with an eccentric off-centred outlet, different flow patterns were observed when the outlet position is accounting for the distance from the lateral wall and the off-centred shift, using the geometrical parameters s and e, respectively. The results showed that the self-similar velocity and volume fraction profiles can be maintained using s instead of e. For the case where the outlet touches the lateral wall of the hopper ($s = 0$), both the velocity and volume fraction profiles exhibit asymmetric behavior. By considering the eccentric location of outlets, a unified expression for

predicting the discharge rate is derived by scaling the velocity and volume fraction. The discharge rate estimated by the proposed relations is in quite good agreement with that obtained directly from DEM simulations. In addition, the discharge rate corresponding to the extreme location of the outlet ($s = 0$) is higher than that of other cases.

In conclusion, the present analysis of self-similarity could provide an approach to describe the discharge of granular matter. The analysis of granular flow in a rectangular hopper with eccentric outlets provides a basis for understanding similar systems of discrete media and extending the centric case to multi-outlet hoppers. In future studies, we intend to focus on the influences of flow configuration, air phase and heat transfer on discharge rate, notably by considering air-particle interactions and drag forces in granular flow analyses.

Acknowledgments

This work was supported financially by the Department of Science and Technology of Jilin Province of China (Grant No. 20220508005RC), Opening fund of State Key Laboratory of Geohazard Prevention and Geoenvironment Protection (Chengdu University of Technology) (Grant No. SKLGP2022K015), National Natural Science Foundation of China (No. 52130001), State Key Laboratory of Geohazard Prevention and Geoenvironment Protection Independent Research Project (No. SKLGP2021Z024).

References

[1] L.H. Luu, G. Noury, Z. Benseghier, P. Philippe, Hydro-mechanical modeling of sinkhole occurrence processes in covered karst terrains during a flood, Eng Geol. 260 (2019) 105249. https://doi.org/10.1016/j.enggeo.2019.105249.

[2] J. Fan, L.-H. Luu, G. Noury, P. Philippe, DEM–LBM numerical modeling of submerged cohesive granular discharges, Granul Matter. 22 (2020) 66. https://doi.org/10.1007/s10035-020-01035-9.

[3] P.W. Cleary, M.L. Sawley, DEM modelling of industrial granular flows: 3D case studies and the effect of particle shape on hopper discharge, Appl Math Model. 26 (2002) 89–111. https://doi.org/10.1016/S0307-904X(01)00050-6.

[4] C. González-Montellano, F. Ayuga, J.Y. Ooi, Discrete element modelling of grain flow in a planar silo: influence of simulation parameters, Granul Matter. 13 (2011) 149–158. https://doi.org/10.1007/s10035-010-0204-9.

[5] C. González-Montellano, Á. Ramírez, E. Gallego, F. Ayuga, Validation and experimental calibration of 3D discrete element models for the simulation of the discharge flow in silos, Chem Eng Sci. 66 (2011) 5116–5126. https://doi.org/10.1016/j.ces.2011.07.009.

[6] C.J. Coetzee, D.N.J. Els, Calibration of discrete element parameters and the modelling of silo discharge and bucket filling, Comput Electron Agric. 65 (2009) 198–212. https://doi.org/10.1016/j.compag.2008.10.002.

[7] P. Le Grognec, S. Laidaoui, P. Aussillous, M. Djermane, B. Dalloz-Dubrujeaud, Discharge flow of granular media from rectangular silos: role of an obstacle and modelling by an orifice at the corner, Mechanics and Industry. 21 (2020) 516. https://doi.org/10.1051/meca/2020048.

[8] I. Zuriguel, A. Janda, A. Garcimartín, C. Lozano, R. Arévalo, D. Maza, Silo clogging reduction by the presence of an obstacle, Phys Rev Lett. 107 (2011) 278001. https://doi.org/10.1103/PhysRevLett.107.278001.

[9] X. Zhang, S. Zhang, G. Yang, P. Lin, Y. Tian, J.F. Wan, L. Yang, Investigation of flow rate in a quasi-2D hopper with two symmetric outlets, Phys Lett A. 380 (2016) 1301–1305. https://doi.org/10.1016/j.physleta.2016.01.046.

[10] D. Méndez, R.C. Hidalgo, D. Maza, The role of the hopper angle in silos: experimental and CFD analysis, Granul Matter. 23 (2021) 34. https://doi.org/10.1007/s10035-021-01094-6.

[11] I. Zuriguel, D.R. Parisi, R.C. Hidalgo, C. Lozano, A. Janda, P.A. Gago, J.P. Peralta, L.M. Ferrer, L.A. Pugnaloni, E. Clément, D. Maza, I. Pagonabarraga, A. Garcimartín, Clogging transition of many-particle systems flowing through bottlenecks, Sci Rep. 4 (2014) 7324. https://doi.org/10.1038/srep07324.

[12] I. Zuriguel, A. Garcimartín, D. Maza, L.A. Pugnaloni, J.M. Pastor, Jamming during the discharge of granular matter from a silo, Phys Rev E Stat Nonlin Soft Matter Phys. 71 (2005) 051303. https://doi.org/10.1103/PhysRevE.71.051303.

[13] W.A. Beverloo, H.A. Leniger, J. Van De Velde, The flow of granular solids

through orifices, Chem Eng Sci. 15 (1961) 260–286. https://doi.org/10.1016/0009-2509(61)85030-6.

[14] T.J. Wilson, C.R. Pfeifer, N. Meysingier, D.J. Durian, Granular discharge rate for submerged hoppers, Papers in Physics. 6 (2014) 060009. https://doi.org/10.4279/PIP.060009.

[15] A. Anand, J.S. Curtis, C.R. Wassgren, B.C. Hancock, W.R. Ketterhagen, Predicting discharge dynamics from a rectangular hopper using the discrete element method (DEM), Chem Eng Sci. 63 (2008) 5821–5830. https://doi.org/10.1016/j.ces.2008.08.015.

[16] J.R. Darias, D. Gella, M.E. Fernández, I. Zuriguel, D. Maza, The hopper angle role on the velocity and solid-fraction profiles at the outlet of silos, Powder Technol. 366 (2020) 488–496. https://doi.org/10.1016/j.powtec.2020.02.061.

[17] Q.C. Yu, N. Zheng, Q.F. Shi, Clogging of granular materials in a horizontal hopper: Effect of outlet size, hopper angle, and driving velocity, Phys Rev E. 103 (2021) 052902. https://doi.org/10.1103/PhysRevE.103.052902.

[18] J.E. Hilton, P.W. Cleary, Granular flow during hopper discharge, Phys Rev E. 84 (2011) 011307. https://doi.org/10.1103/PhysRevE.84.011307.

[19] M.E.Myers, M. Sellers, Rate of discharge from wedge-shaped hoppers， Chemical engineering, tripos part 2, Research Project Report, University of Cambridge. (1971).

[20] M. Benyamine, P. Aussillous, B. Dalloz-Dubrujeaud, Discharge flow of a granular media from a silo: effect of the packing fraction and of the hopper angle, EPJ Web Conf. 140 (2017) 03043. https://doi.org/10.1051/epjconf/201714003043.

[21] R. Brown, J. Richards, Principles of Powder Mechanics, Pergamon, 1970. https://doi.org/10.1017/CBO9780511600043.

[22] R.L. Brown, Minimum energy theorem for flow of dry granules through apertures, Nature. 191 (1961) 458–461. https://doi.org/10.1038/191458a0.

[23] A. Bhateja, S. Jain, Self-similar velocity and solid fraction profiles in silos with eccentrically located outlets, Physics of Fluids. 34 (2022) 043306. https://doi.org/10.1063/5.0083421.

[24] R. Maiti, S. Meena, P.K. Das, G. Das, Flow field during eccentric discharge from quasi-two-dimensional silos-extension of the kinematic model with validation, AIChE Journal. 62 (2016) 1439–1453. https://doi.org/10.1002/aic.15149.

[25] Y. Wang, F. Jia, J. Zhang, Y. Han, P. Chen, A. Li, J. Fei, W. Feng, X. Hao, S. Shen, Model construction method of discharge rate of eccentric silo, Powder Technol. 405 (2022) 117555. https://doi.org/10.1016/j.powtec.2022.117555.

[26] J. Fan, L.H. Luu, P. Philippe, G. Noury, Discharge rate characterization for submerged grains flowing through a hopper using DEM-LBM simulations, Powder Technol. 404 (2022) 117421. https://doi.org/10.1016/j.powtec.2022.117421.

[27] L.A. Fullard, E.C.P. Breard, C.E. Davies, A.J.R. Godfrey, M. Fukuoka, A. Wade,

J. Dufek, G. Lube, The dynamics of granular flow from a silo with two symmetric openings, Proceedings of the Royal Society A: Mathematical, Physical and Engineering Sciences. 475 (2019) 20180462. https://doi.org/https://doi.org/10.1098/rspa.2018.0462.

[28] Y. Cheng, J.D. Treado, B. Lonial, P. Habdas, E.R. Weeks, M.D. Shattuck, C.S. O'Hern, Hopper flows of deformable particles, Soft Matter. 18 (2022) 8071. https://doi.org/10.1039/d2sm01079h.

[29] S. Wang, M. Zhuravkov, S. Ji, Granular flow of cylinder-like particles in a cylindrical hopper under external pressure based on DEM simulations, Soft Matter. 16 (2020) 7760–7777. https://doi.org/10.1039/c9sm02435b.

[30] R. Arévalo, Collisional regime during the discharge of a two-dimensional silo, Phys Rev E. 105 (2022) 044901. https://doi.org/10.1103/PhysRevE.105.044901.

[31] Z. Zou, P. Ruyer, P.Y. Lagrée, P. Aussillous, Discharge of a silo through a lateral orifice: Role of the bottom inclination versus friction, Phys Rev E. 102 (2020) 052902. https://doi.org/10.1103/PhysRevE.102.052902.

[32] S.D. Liu, Z.Y. Zhou, R.P. Zou, D. Pinson, A.B. Yu, Flow characteristics and discharge rate of ellipsoidal particles in a flat bottom hopper, Powder Technol. 253 (2014) 70–79. https://doi.org/10.1016/j.powtec.2013.11.001.

[33] S. Ji, S. Wang, Z. Peng, Influence of external pressure on granular flow in a cylindrical silo based on discrete element method, Powder Technol. 356 (2019) 702–714. https://doi.org/10.1016/j.powtec.2019.08.083.

[34] Z. Zhang, Y. Liu, B. Zheng, R. Li, P. Sun, Discharge characteristics of binary particles in a rectangular hopper with inclined bottom, Comput Part Mech. 8 (2021) 315–324. https://doi.org/10.1007/s40571-020-00332-7.

[35] P.A. Cundall, O.D.L. Strack, A discrete numerical model for granular assemblies, Géotechnique. 29 (1979) 47–65. https://doi.org/10.1680/geot.1979.29.1.47.

[36] A. di Renzo, F. Paolo Di Maio, An improved integral non-linear model for the contact of particles in distinct element simulations, Chem Eng Sci. 60 (2005) 1303–1312. https://doi.org/10.1016/j.ces.2004.10.004.

[37] Q. Gao, Y. Chen, C. Zhao, Self-similarity of density and velocity profiles in a 2D hopper flow of elliptical particles: Discrete element simulation, Powder Technol. 402 (2022) 117338. https://doi.org/10.1016/j.powtec.2022.117338.

[38] R.M. Nedderman, C. Laohakul, The thickness of the shear zone of flowing granular materials, Powder Technol. 25 (1980) 91–100. https://doi.org/https://doi.org/10.1016/0032-5910(80)87014-8.

[39] A. Janda, I. Zuriguel, D. Maza, Flow rate of particles through apertures obtained from self-similar density and velocity profiles, Phys Rev Lett. 108 (2012) 248001. https://doi.org/10.1103/PhysRevLett.108.248001.

[40] Y. Zhou, P. Ruyer, P. Aussillous, Discharge flow of a bidisperse granular media from a silo: Discrete particle simulations, Phys Rev E. 92 (2015) 062204. https://doi.org/10.1103/PhysRevE.92.062204.

[41] Y. Zhou, P.Y. Lagreé, S. Popinet, P. Ruyer, P. Aussillous, Experiments on, and

discrete and continuum simulations of, the discharge of granular media from silos with a lateral orifice, J Fluid Mech. 829 (2017) 459–485. https://doi.org/10.1017/jfm.2017.543.

[42] R. Blanco-Rodríguez, R.C. Hidalgo, G. Pérez-Ángel, D. Maza, Critical numerical analysis of quasi-two-dimensional silo-hopper discharging, Granul Matter. 23 (2021) 86. https://doi.org/10.1007/s10035-021-01159-6.

[43] H.F. Rose, T. Tanaka, Rate of discharge of granular materials from bins and hoppers, Engineer. 208 (1959) 465 – 469.